ARTICLE

Constructing TiO$_2$/g-C$_3$N$_4$/Single-Walled Carbon Nanotube Hydrogel for Synergistic Solar Evaporation and Photocatalytic Organic Pollutant

Junxiao Qiu[1,2] and Sanmei Liu[3,4,*]

[1]Jiangxi Provincial Key Laboratory of Flexible Electronics, Jiangxi Science and Technology Normal University/Nanchang Jiaotong Institute, Nanchang, 330013, China

[2]School of Pharmacy, Jiangxi Science and Technology Normal University, Nanchang, 330013, China

[3]School of Chemistry and Chemical Engineering, Jiangxi Science and Technology Normal University, Nanchang, 330013, China

[4]Centre for Analysis and Testing, Jiangxi Science and Technology Normal University, Nanchang, 330013, China

*Corresponding Author: Sanmei Liu. Email: 1020240102@jxstnu.edu.cn

ABSTRACT

Integration of solar-driven interfacial evaporation and photocatalysis is one of the most promising technologies for generating fresh water and removing pollutants. In this work, TiO$_2$/g-C$_3$N$_4$ photocatalysis is loaded on a hydrogel containing single-walled carbon nanotube (SWCNT). Due to the excellent water evaporation channel of hydrogel and the excellent photothermal conversion performance of SWCNT, as well as the good visible light absorption ability of TiO$_2$/g-C$_3$N$_4$, TiO$_2$/g-C$_3$N$_4$/SWCNT hydrogel exhibits good hydrothermal evaporation and photocatalytic activity. The optimum water evaporation rate of 1.43 kg m^{-2} h^{-1}. In particular, the optimized TiO$_2$/g-C$_3$N$_4$/SWCNT hydrogel can also remove more than 90% methylene blue (MB) within 120 min. Moreover, the TiO$_2$/g-C$_3$N$_4$/SWCNT hydrogel shows good photocatalytic stability after five cycles. Furthermore, the radical trapping experiment is also performed. The photogenerated $\cdot O_2^-$ and $\cdot OH^-$ plays a critical role in MB degradation. This work will provide guidance for the rational design of multifunctional photothermal materials. TiO$_2$/g-C$_3$N$_4$/SWCNT hydrogel presents a promising methodology to boost practical applications for seawater desalination and sewage purification.

KEYWORDS

Interfacial evaporation; photocatalysis; TiO$_2$/g-C$_3$N$_4$/SWCNT hydrogel; methylene blue

1 Introduction

The rapid population growth, worsening pollution, and increasingly severe weather have exacerbated the global water and energy crises. Currently, the shortage of freshwater resources worldwide poses a severe threat to the stability of ecosystems and human health [1–3]. Many people, especially those in remote and rural areas, lack the infrastructure needed to consistently access safe drinking water. Consequently, developing cost-effective wastewater treatment technologies has been a focus of research. Utilizing renewable solar energy through interfacial solar steam evaporation technology has

shown great potential for seawater desalination [4–7] and wastewater treatment [8–11]. Although solar photothermal technology offers promising solutions for wastewater issues, traditional evaporators struggle to efficiently treat wastewater. To address this, researchers have combined photothermal evaporators with photocatalysts to achieve both efficient water evaporation and wastewater treatment. For example, Li et al. [12] developed an Ag/MXene membrane that leverages photothermal and photocatalytic synergy to degrade heavy metal ions and organic pollutants during wastewater treatment; Miao et al. [13] designed a metal-organic frameworks (MOFs)-derived C/TiO_2 composite material that simultaneously performs photothermal and photocatalytic functions, enabling solar-driven freshwater production and degradation of organic pollutants in wastewater. As research progresses, photothermal-photocatalytic materials have been demonstrated to degrade volatile organic compounds (VOCs) in distilled water [14]. Additionally, solar-driven photocatalytic evaporators offer the potential for multifunctional applications, achieving dual [15] or even triple benefits [16].

Owing to their three-dimensional network structures with activated water states, excellent mechanical/optical/electronic properties, and multi-scale tunability, hydrogels have gained widespread applications in various fields such as bioelectronics [17–19], biomedical engineering [20], energy conversion [21], strain sensors [22], electrochromics [23], soft robotics [24,25], etc. Particularly, various hydrogel-based evaporators have also been developed for water purification in recent years [6,8,20,21]. For example, Wang et al. [14] developed an MXene/CdS photothermal-photocatalytic hydrogel for efficient solar water evaporation and VOC degradation. Zhao et al. [26] designed a galactomannan/graphene oxide/Fe_3O_4 hydrogel evaporator for solar-driven water evaporation and simultaneous photothermal power generation. Zheng et al. [27] created a magnetically controlled, wind-resistant Janus biomass composite hydrogel with desalination capabilities for the purification of polluted seawater. Lyu et al. [28] developed a simple, low-cost macroporous hydrogel for high-performance atmospheric water harvesting (AWH). Therefore, hydrogels integrating photothermal and photocatalytic effects hold significant potential in this field.

TiO_2, due to its low cost and environmental friendliness, is a potential photocatalyst. However, it can only absorb ultraviolet light, and the rapid recombination of photogenerated carriers significantly reduces its photocatalytic activity [29–31]. To overcome these drawbacks, constructing heterojunctions is an ideal strategy to mitigate the rapid recombination of photogenerated carriers. Since $g\text{-}C_3N_4$ exhibits good visible light absorption, combining TiO_2 with $g\text{-}C_3N_4$ can effectively reduce photogenerated carrier recombination [32–35]. There are relevant studies on this topic, such as the work by Yu et al. [36], who developed an advanced 2D/3D $g\text{-}C_3N_4/TiO_2@MnO_2$ multifunctional separation membrane for light-driven sustainable water purification. Yang et al. [37] designed a hollow octahedral MOF-derived TiO_2 structure combined with ultrathin porous $g\text{-}C_3N_4$, enhancing the degradation efficiency of brewing wastewater.

Given the above analysis, this paper demonstrates that $TiO_2/g\text{-}C_3N_4$ loaded on a hydrogel matrix can achieve efficient solar-driven evaporation and organic pollutant degradation. By incorporating SWCNTs with broad-spectrum absorption and $TiO_2/g\text{-}C_3N_4$ photocatalytic heterojunction, a hydrogel with dual functionalities of photocatalytic degradation and interfacial evaporation is developed. The prepared $TiO_2/g\text{-}C_3N_4/SWCNT$ composite hydrogel exhibited excellent light absorption across the full spectrum (approximately 98.9%), efficient photothermal conversion (35.9°C), and a water evaporation rate of 1.43 kg m^{-2} h^{-1}. Notably, the hydrogel exhibited a lower evaporation enthalpy than pure water (as low as 1144.7 J g^{-1}). The photocatalytic performance of the hydrogel enabled over 90% degradation of pollutants within 120 min, with almost no decline in photocatalytic performance after five cycles. The primary active species for methylene blue (MB) photodegradation are $\cdot O_2^-$ and $\cdot OH^-$.

2 Experimental Section

Materials: N,N'-Methylenebis (acrylamide) (MBAA, 99%), ammonium persulfate (APS, ≥98%), acrylamide (AM, 99.0%), melamine (99%), and titanium oxide (TiO$_2$, 98%) were obtained from Aladdin (Shanghai, China). N,N,N',N'-Tetramethylethylenediamine (TEMED, 99%) was obtained from J&K Scientific (Beijing, China). Single-walled carbon nanotube (SWCNT) aqueous dispersion (9–10 wt.%) was obtained from XFNano (Nanjing, China). All other reagents were analytical grade and directly employed without further purification.

Preparation of graphitic carbon nitride (g-C$_3$N$_4$): g-C$_3$N$_4$ was prepared by direct thermal polymerization. Specifically, 5 g of melamine was placed into a crucible, covered with a lid, and heated in a muffle furnace at a rate of 15°C/min to 550°C. The temperature was maintained for 4 h, and then the sample was cooled to room temperature. After cooling, the product was removed and ground into a powder in a mortar for future use.

Preparation of single catalyst hydrogel: First, 0.3 g of TiO$_2$ nanoparticle/g-C$_3$N$_4$ powder was added to 10 mL of deionized water, stirred thoroughly, and then sonicated for 30 min to form a homogeneous aqueous solution. Subsequently, 0.027 g of a diluted aqueous dispersion of single-walled carbon nanotubes (4.5–5 wt.%) was added and stirred well to form dispersion A. Then, 1.1 g of AM monomer was added to dispersion A, stirred until dissolved, and 100 μL of APS (10 wt.%) initiator solution and 0.0125 g of MBAA crosslinker were added to form solution B. The stirred dispersion of solution B was then sonicated for 10 min to form a homogeneous dispersion. Afterward, 50 μL of TEMED catalyst was added while stirring, and after stirring for 1 min, the mixture was transferred to a mold for gelation. After the gelation was completed at room temperature, the hydrogel was demolded and soaked in deionized water for more than 48 h to remove residual substances. It is noteworthy that the TiO$_2$/SWCNT and g-C$_3$N$_4$/SWCNT hydrogels corresponded to TSH and CSH, respectively.

Preparation of composite catalyst hydrogel: First, 0.3 g of TiO$_2$ nanoparticle and 0.3 g of g-C$_3$N$_4$ powder were added to 10 mL of deionized water, stirred thoroughly, and then sonicated for 30 min to form a homogeneous aqueous solution. Subsequently, 0.027 g of a diluted aqueous dispersion of single-walled carbon nanotubes (4.5–5 wt.%) was added and stirred well to form dispersion A. Then, 1.1 g of AM monomer was added to dispersion A, stirred until dissolved, and 100 μL of APS (10 wt.%) initiator solution and 0.0125 g of MBAA crosslinker were added to form solution B. The stirred dispersion of solution B was then sonicated for 10 min to form a homogeneous dispersion. Afterward, 50 μL of TEMED catalyst was added while stirring, and after stirring for 1 min, the mixture was transferred to a mold for gelation. After the gelation was completed at room temperature, the hydrogel was demolded and soaked in deionized water for more than 48 h to remove residual substances. It is noteworthy that in the TiO$_2$/g-C$_3$N$_4$/SWCNT composite hydrogel, the weight ratios of TiO$_2$ to g-C$_3$N$_4$ were 1:1, 1:2, and 2:1, corresponding to TCSH-1, TCSH-2, and TCSH-3, respectively.

Characterizations: The surface morphology and chemical element distribution of TSH, CSH, and TCSH-1 hydrogels were characterized using using a scanning electron microscope (SEM, SU8600, Hitachi, Tokyo, Japan) equipped with an X-ray energy dispersive spectrometer (EDS, ELECT SUPER(C5), EDAX, Commonwealth of Pennsylvania, US). The TiO$_2$ and g-C$_3$N$_4$ powders were analyzed by X-ray photoelectron spectroscopy using an X-ray diffractometer (XRD, Empyrean, MalvernPanalytical, Malvern, UK). The diffuse reflectance properties of the prepared samples were measured using an ultraviolet-visible-near-infrared spectrophotometer (TP720, Tianjin Toupu Instrument Co., Tianjin, China) with an integrating sphere unit and an automatic reflectance measurement unit, and the obtained spectra were corrected for baseline/blank and black. The absorbance (*A*) was obtained through the Eq. (1):

$$A = 1 - T - R \tag{1}$$

where R and T are the reflectance and transmittance of the hydrogel, respectively.

Photocatalytic performance measurements: The photocatalytic performance of the hydrogels was evaluated using methylene blue (MB) at a concentration of 10 g L^{-1} as a model. The light intensity was maintained at one sun (1 kW m^{-2}), with a solar simulator as the light source (CEL-HXUV300-T3, Education Au-light Co., Beijing, China). The prepared 3D columnar hydrogels were cut into small pieces and placed in the methylene blue solution before irradiation, kept in the dark for 60 min to achieve adsorption-desorption equilibrium. Subsequently, samples (3 mL) were taken every 15 min and measured using a UV-Vis-NIR spectrophotometer (TP720, Tianjin Toupu Instrument Co., Tianjin, China). Moreover, the degradation efficiency (D_e) was calculated based on the Eq. (2) [38,39]:

$$D_e = 1 - C/C_0 \tag{2}$$

where C_0 denotes the initial concentration, and C is the concentration of the solution in different periods. We further evaluate the photocatalytic efficiency based on the pseudo-first-order model according to the Eq. (3) [40]:

$$-\ln(C/C_0) = kt \tag{3}$$

where k is related to the constant photodegradation rate.

Solar steam generation performance measurements: The solar steam generation performance of the hydrogels was tested using a solar simulator with an AM1.5 filter (CEL-HXUV300-T3, Education Au-light Co., Beijing, China). The solar flux was measured by an automatic optical power meter (CEL-NP2000-2A, Education Au-light Co., Beijing, China). The mass change during the evaporation process was monitored in real-time using an electronic analytical balance (Sartorius BAS223, accurate to 1 mg). The surface temperature and infrared thermograms of the hydrogels were monitored in real-time using an infrared thermal imager (HM-TPH21Pr0-3AQF, HIKMICRO, Hangzhou, China). During the tests, the ambient humidity and temperature were ~60% and ~25°C, respectively. Additionally, the evaporation rate (E_R) and equivalent evaporation enthalpy (E_{equ}) were calculated based on the Eqs. (4) and (5) [41]:

$$E_R = d_m/(S * d_t) \tag{4}$$

where d_m denotes to the mass change by using hydrogel as the evaporator for 1 h, S is the evaporation area of hydrogel, and d_t is evaporation time.

$$E_{equ} = \frac{E_0 m_0}{m_g} \tag{5}$$

where E_0 and m_0 are the evaporation enthalpy and mass change of bulk water; m_g is the mass change of hydrogel.

Conductivity and salinity measurements: In the conductivity range of 0.001 to 0.01 wt.‰, the salinity of NaCl solutions exhibits a strong linear correlation with electrical conductivity. A standard curve was established by testing the conductivity of different brines with a conductivity controller (A10CD-AA1, Shanghai Kuosi Electronics Co., Shanghai, China) and used to calculate the salinity of pure water evaporated from simulated seawater by TCSH-1. The conductivity of at least three parallel samples is measured and averaged to accurately determine the salinity.

3 Results and Discussion

As shown in Fig. 1a, the hydrogel prepared in the experiment has a three-dimensional columnar structure, designed to increase the evaporation area and thereby enhance the evaporation rate of the hydrogel. TiO$_2$ nanoparticles and g-C$_3$N$_4$ nanosheet dual catalysts are integrated into the

hydrogel matrix. The characteristic macroporous structure of the hydrogel not only enables multi-level refraction and diffraction of light within the gel network, thereby enhancing light absorption, but also allows for rapid water absorption and transport (Fig. 1b). In addition, this design specifically addresses the drawback of TiO_2, which can only absorb ultraviolet light, and its reduced photocatalytic efficiency due to rapid photogenerated carrier recombination. Since g-C_3N_4 has well visible light absorption, the heterojunction constructed by the dual catalysts can improve the efficiency of the photocatalyst (Fig. 1c). The incorporation of photocatalytic functionality not only enables efficient sewage purification but also prevents the contamination of bulk water during the evaporation process. Such hydrogels hold promise for multifunctional applications in solar-powered water purification systems.
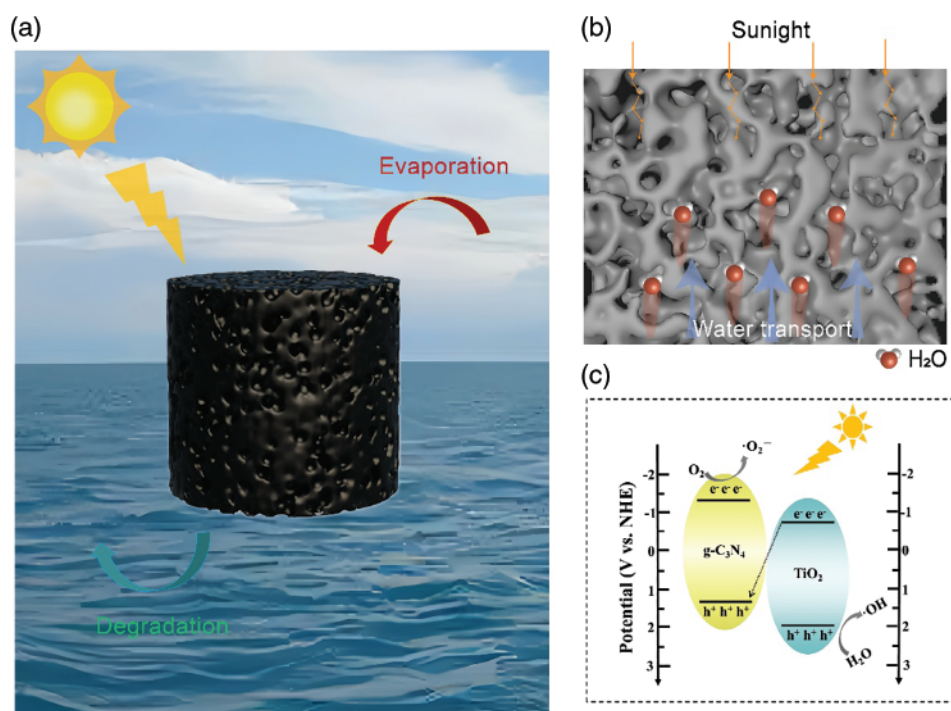

Figure 1: Schematic diagram of hydrogel evaporation and photocatalysis. (a) Schematic diagram of TiO_2/g-C_3N_4/SWCNT (TCSH-1) and its advantages in solar-driven water purification: photothermal evaporation and photocatalytic degradation. (b) Schematic diagram of the porous structure of the hydrogel, illustrating the multi-level refraction and diffraction of light within the gel network, as well as the rapid absorption of water from the bottom towards the top. (c) Schematic diagram of the mechanism of TCSH-1 photocatalytic degradation of MB

TiO_2 and g-C_3N_4, as typical photocatalysts, are now widely applied. In this study, g-C_3N_4 powder is synthesized by a direct thermal polymerization method, resulting in a pale yellow color. The microstructure and crystal structure of the two solid catalysts are further explored through Scanning Electron Microscopy (SEM) and X-ray Diffraction (XRD). As shown in Fig. S1, the TiO_2 and g-C_3N_4 solids exhibit different morphological structures at 2 µm. The purchased TiO_2 appears as nanoparticles under microscopic observation, while the g-C_3N_4 obtained by thermal polymerization exhibits a sheet-like structure. Further crystal structure analysis is performed using XRD. As shown in Fig. S2, the diffraction peaks at $2\theta = 13.5°$ and $27.4°$ correspond to the (100) and (002) crystal planes of the g-C_3N_4 standard sample card (JCPDS 87-1526), respectively. The diffraction peak at 13.5° is attributed to the tris-s-triazine rings, and the sharp diffraction peak at 27.4° is caused by the

stacking of aromatic heterocycles. This indicates that g-C_3N_4 is successfully prepared by the direct thermal polymerization method and that the prepared g-C_3N_4 possesses good purity and crystallinity. Subsequently, the samples of TiO_2/g-C_3N_4 loaded on the hydrogel matrix are analyzed using SEM and Energy Dispersive X-ray Spectroscopy (EDS). The results show that the photocatalyst is successfully loaded in the hydrogel, displaying the characteristic porous structure of the hydrogel (Fig. 2).
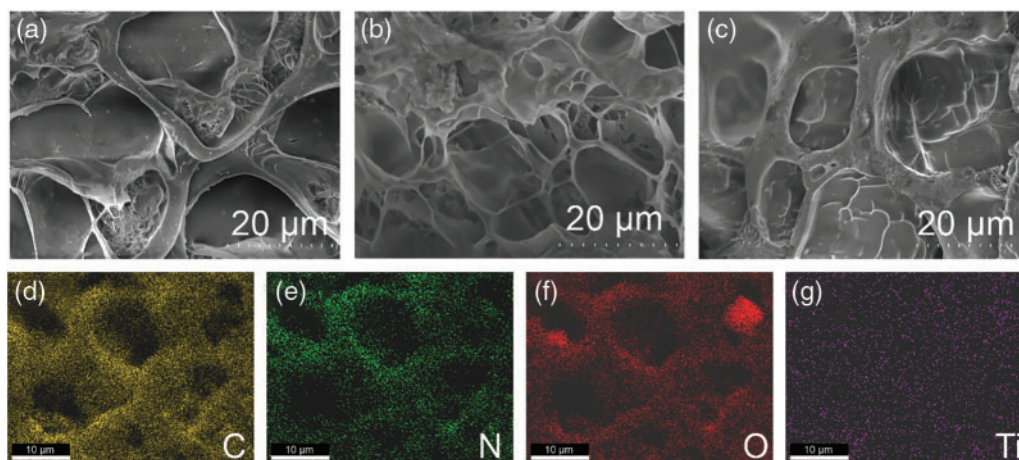

Figure 2: Microstructure and elemental distribution. SEM images of (a) TSH, (b) CSH, (c) TCSH-1, (d) elemental mapping images of C, (e) N, (f) O, and (g) Ti

Excellent light absorption across the full spectrum is essential for achieving efficient photothermal conversion and solar-driven evaporation performance in hydrogels. As shown in Fig. 3a, the prepared single and composite photocatalytic hydrogels exhibit superior light absorption across the entire spectrum (with an absorption rate greater than 98.8%), with negligible light loss. Notably, the light absorption rate of TSH reaches 99.9%, outperforming CSH and TCSH-1. The primary reason for this is that the reflectivity of the TCSH-1 hydrogel across the full spectrum is higher than that of the other two single-catalyst hydrogels (Fig. 3b). Furthermore, we investigate the wetting properties of TSH, CSH, and TCSH-1 through water contact angle measurements. The contact angle of the TCSH-1 hydrogel rapidly decreases to 12.87°, facilitating the dynamic migration of water molecules to the evaporator surface (Fig. S3). As depicted in Fig. 3d,e, the water evaporation performance of TSH, CSH, and TCSH-1 is evaluated by recording the mass change of water under 1 kW m^{-2} solar irradiation over 60 min. As the irradiation time increases, the mass change of water in each hydrogel exhibits a linear increase, with the CSH sample showing the highest evaporation rate, approximately 1.63 kg m^{-2} h^{-1}. The water evaporation rate of the prepared TCSH-1 shows a decreasing trend with the increase in the number of photocatalysts in the hydrogel components. Furthermore, the different evaporation rates of the hydrogels are verified by testing the equivalent enthalpy of evaporation. Specifically, the evaporation rate is recorded by placing the hydrogels under dark conditions, and the corresponding equivalent enthalpy of evaporation is calculated using Eq. (5). The results indicate that the obtained enthalpy of evaporation correlates well with the hydrogel evaporation rate results, with CSH having the lowest equivalent enthalpy of evaporation, at 1144.7 J g^{-1} (Fig. 3c). Notably, the equivalent enthalpy of evaporation of the prepared hydrogels is significantly lower than that of pure water (2450 J g^{-1}). The photothermal conversion efficiency of these hydrogels is further demonstrated by monitoring the interface temperature changes of the hydrogels under illumination using infrared imaging technology. Remarkably, the temperature of the hydrogels rapidly rises above 30°C within the first 10 min of light exposure, followed by a slow increase to 35.9°C. The rapid decrease in surface

temperature in the absence of light further confirms the high photothermal conversion capability of the hydrogels (Fig. 3f,g).
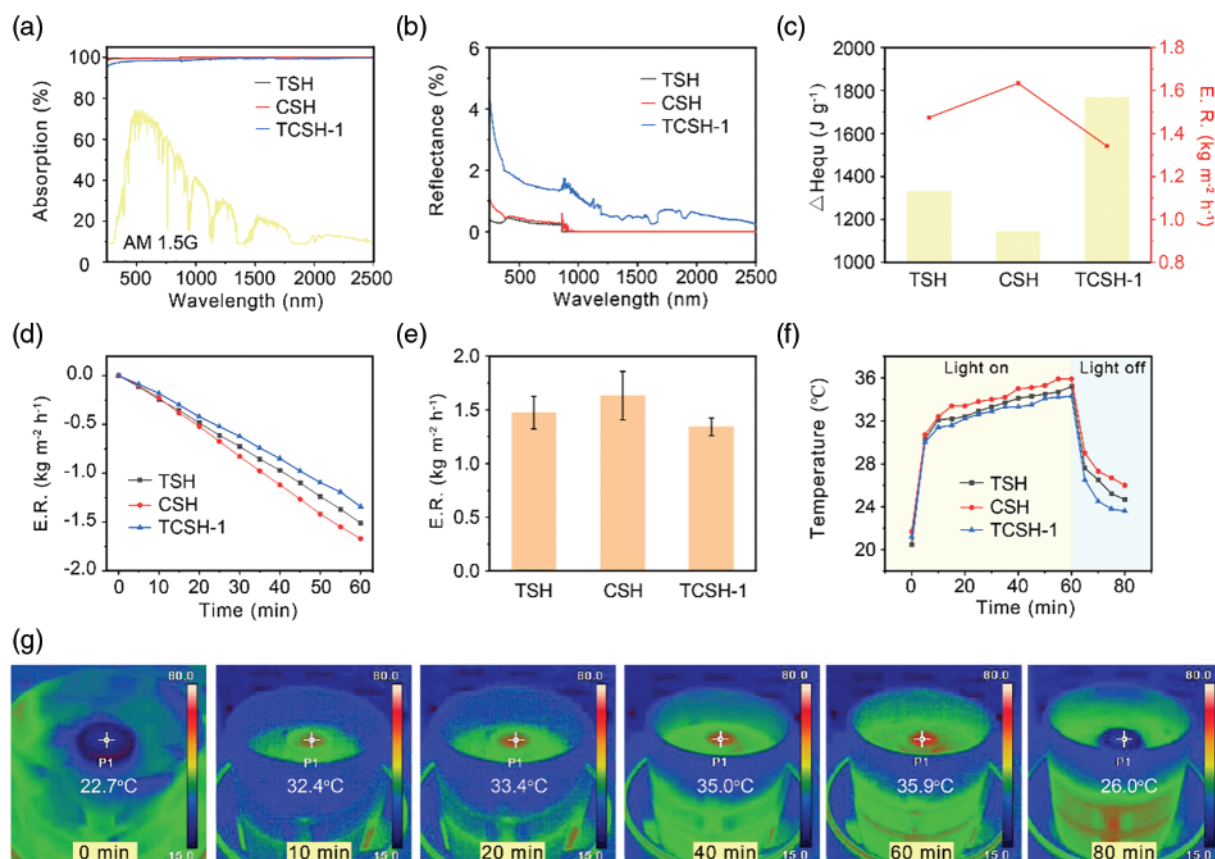

Figure 3: The light absorption and photothermal conversion properties of hydrogels. The absorbance (a) and reflectance (b) of TSH, CSH, and TCSH-1 hydrogels across the full spectral range. (c) The relationship between the equivalent evaporation enthalpy and the evaporation rate of TSH, CSH, and TCSH-1 hydrogels. (d) The change in water mass over time for TSH, CSH, and TCSH-1 hydrogels under one sun illumination, with corresponding evaporation rate (e) and temperature response (f). (g) The evaporation experiment using CSH floating on bulk water, is conducted at irradiation times of 0, 10, 20, 40, 60, and 80 min, with corresponding photographs and infrared images

The long-term stability of materials is essential for ensuring the sustainable and efficient operation of water purification processes. To evaluate the stability of the TCSH-1 hydrogel, it is subjected to a cyclic test in 3.5 wt.% simulated seawater for seven consecutive cycles (Fig. 4a). After repeated swelling-evaporation processes, the evaporation performance of the hydrogel remains consistently at 2.03 kg m^{-2} h^{-1}. Furthermore, the evaporation performance of the TCSH-1 hydrogel evaporator is tested under outdoor conditions to assess its practical performance in a real-world environment. As shown in Fig. S4, a fully automatic optical power meter records the solar power density in Nanchang from 9:00 a.m. to 16:00 p.m. on 23rd September. The weather on that day is cloudy to overcast, with a light breeze (wind speed 3–4 level), and the hourly evaporation rates are displayed in Fig. 4b.

Next, the performance of the hydrogel in seawater desalination and wastewater purification is evaluated. Three different simulated seawater samples—World Sea (average salinity 35 wt.‰), Bohai Sea (moderate salinity, 70 wt.‰), and Dead Sea (highest salinity, 200 wt.‰)—are purified. After purification, the salinity of these samples decreases by 3 to 4 orders of magnitude, as shown in

Figs. 4c and S5. Additionally, the purified water meets the drinking water standards of the World Health Organization (WHO, 1 wt.‰) and the Environmental Protection Agency (EPA, 0.5 wt.‰). Inductively coupled plasma mass spectrometry (ICP-MS) is used to measure the concentrations of salt ions, including Na^+, Mg^{2+}, K^+, and Ca^{2+}, in the evaporated water. As depicted in Fig. 4d, the concentrations of major salt ions decrease by more than three orders of magnitude after purification, demonstrating the high desalination efficiency of TCSH-1.
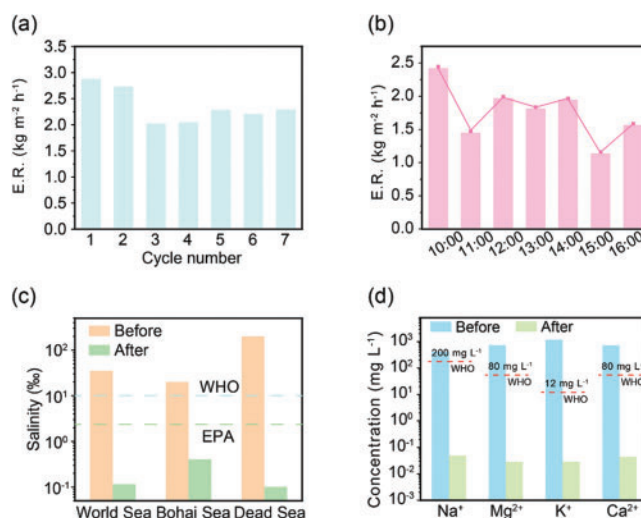

Figure 4: The practical application performance of hydrogels. (a) The TCSH-1 hydrogel undergoes continuous evaporation testing in 3.5 wt.% simulated seawater. (b) The evaporation performance of the hydrogel evaporator is evaluated under outdoor conditions. (c) Salinity of the simulated seawater samples is measured before and after desalination. (d) The concentrations of typical salt cations (Na^+, Mg^{2+}, K^+, and Ca^{2+}) in the seawater samples are analyzed before and after purification

The photocatalytic efficiency of the prepared hydrogel is evaluated through the photodegradation test of a typical organic pollutant, methylene blue (MB). First, the hydrogel is placed under dark conditions for 60 min to achieve adsorption-desorption equilibrium, followed by a 120-min photocatalytic degradation test of MB. The results indicate that TCSH-1 exhibits the highest degradation efficiency (Fig. 5a). As shown in Fig. 5b, kinetic analysis reveals that the rate constants (k values) for TSH, CSH, TCSH-1, TCSH-2, and TCSH-3 hydrogels are 0.0104, 0.01293, 0.02039, 0.01664, and 0.01311 min^{-1}, respectively. As shown in Table S1, the TCSH-1 hydrogel evaporator exhibits better photothermal evaporation efficiency [42–44]. More notably, TCSH-1 hydrogel is much better than or comparable to those of reported hydrogel based catalysts [45–47]. Therefore, TSH, CSH, and TCSH-1 are selected for subsequent experiments. As shown in Fig. 5c, the UV-visible absorption spectra indicate that the absorption peak of MB at 664 nm significantly decreases over time, suggesting the gradual degradation of MB. As can be seen from Fig. 5d, the catalytic performance of the photocatalyst slightly decreases after five cycles (10 h). Moreover, the SEM morphology of TCSH-1 remains nearly unchanged after five cycles (Fig. S6), indicating that the synthesized TCSH-1 exhibits excellent stability.

The mechanism of photodegradation MB for TCSH-1 is further studied in Fig. 6. Radicals and holes trapping experiments are adopted by adding p-benzoquinone (BQ), disodium ethylenediaminetetraacetate (EDTA-2Na) and isopropyl alcohol (IPA), which using as $\cdot h^+$, $\cdot O_2^-$ and $\cdot OH^-$, respectively (Fig. 6a). As presented in Fig. 6b, a significant effect is observed after adding BQ and IPA for photodegradation activity, implying $\cdot O_2^-$ and $\cdot OH^-$ are dominant active species in photodegradation MB. The optical properties of TSH, CSH, and TCSH-1 are investigated. As seen in Fig. 6c, CSH and

TCSH-1 display the absorption edge in visible light. In order to obtain E_g of TiO_2 and g-C_3N_4, their UV-vis diffusion reflection spectra and Tacu plots are provided in Fig. 6d, and the bandgap of the semiconductor catalysts are obtained according to the Eq. (6) [48,49]:

$$(\alpha h_V)^n = A(h_V - E_g) \tag{6}$$

The E_g of TiO_2 and g-C_3N_4 were 3.1 and 2.74 eV by the straight line to the X axis intercept, respectively.
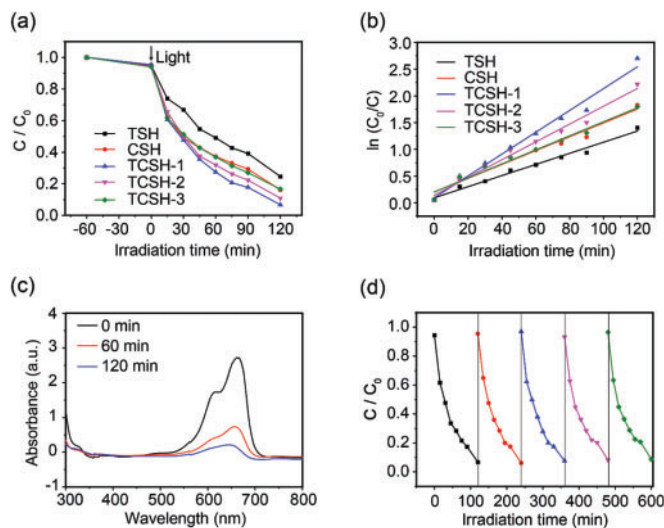

Figure 5: Photocatalytic degradation of MB experiment. (a) Degradation percent and (b) kinetic curves of TSH, CSH, TCSH-1, TCSH-2, TCSH-3. Photodegradation MB for (c) Temporal UV-vis adsorption spectra of TCSH-1. (d) Five cycles of the TCSH-1
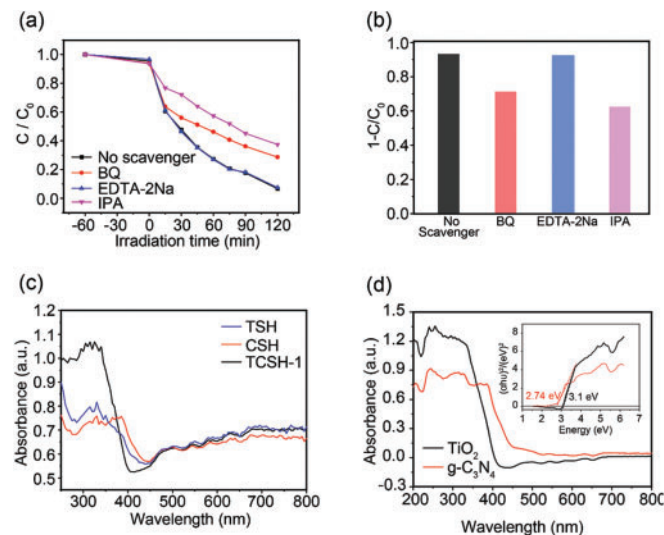

Figure 6: Photocatalytic mechanism investigation. (a) Effect of different scavengers for photodegradation MB in the presence of TCSH-1. (b) Histogram of the conversion of TCSH-1. (c) UV-vis diffusion reflection spectra of TSH, CSH, TCSH-1, and (d) TiO_2, g-C_3N_4 (the inset: is corresponding Tacu plots)

To better understand the mechanism of this photodegradation MB process, the conduction and valence band positions of TiO_2 and $g\text{-}C_3N_4$ are estimated according to reported literature [50]. The process of charge separation and transfer in $TiO_2/g\text{-}C_3N_4/SWCNT$ hydrogel can be illustrated in Scheme S1 according to the above-mentioned results. The electron-hole pairs are generated and the electrons transferred from the VB to the CB when the $TiO_2/g\text{-}C_3N_4/SWCNT$ hydrogel absorbed visible light. Because the $\cdot O_2^-$ and $\cdot OH^-$ as the primary active species for MB degradation, a possible Z type heterojunction between TiO_2 and $g\text{-}C_3N_4$ is proposed, the photogenerated electrons of TiO_2 can be migrated to VB of $g\text{-}C_3N_4$, the electrons in CB of $g\text{-}C_3N_4$ is combined the O_2 to produce $\cdot O_2^-$ and the hole in VB of TiO_2 is combined the H_2O to produce $\cdot OH^-$ to degrade MB. Thus, effective separation of the photogenerated electron-hole pairs are achieved.

4 Conclusions

In summary, $TiO_2/g\text{-}C_3N_4/SWCNT$ hydrogel with solar water evaporation and photocatalytic activity is successfully synthesized. The obtained $TiO_2/g\text{-}C_3N_4/SWCNT$ hydrogel show well water evaporation channel, photothermal conversion, and charge separation efficiency. Due to these merits, the $TiO_2/g\text{-}C_3N_4/SWCNT$ hydrogel demonstrates good water evaporation efficiency and photodegradation performance for MB. Furthermore, the radical trapping experiment is conducted to further understand the mechanism of photodegradation, and the result confirms that the $\cdot O_2^-$ and $\cdot OH^-$ are the main active species for MB degradation. This study is helpful for designing and developing efficient multi-functional photothermal materials.

Author Contributions: The authors confirm contribution to the paper as follows: Writing—review & editing, Writing—original draft, Software, Formal analysis, Data curation, Experiment, Conceptualization: Junxiao Qiu; Writing—review & editing, Writing—original draft, Resources, Supervision, Data curation, Conceptualization, Funding acquisition: Sanmei Liu. All authors reviewed the results and approved the final version of the manuscript.

Availability of Data and Materials: The datasets generated during and analyzed during the current study are available from the corresponding author on reasonable request.

Ethics Approval: Not applicable.

Conflicts of Interest: The authors declare no conflicts of interest to report regarding the present study.

Supplementary Materials: Supplementary material is available online at https://doi.org/10.32604/jpm.2024.057951.

References

1. Shannon MA, Bohn PW, Elimelech M, Georgiadis JG, Mariñas BJ, Mayes AM. Science and technology for water purification in the coming decades. Nature. 2008;452(7185):301–10. doi:10.1038/nature06599.
2. Mekonnen MM, Hoekstra AY. Four billion people facing severe water scarcity. Sci Adv. 2016;2(2):e1500323. doi:10.1126/sciadv.1500323.

3. Lorenzo R, Davide DC, Maria CR, Jampel DA, Paolo D. Global agricultural economic water scarcity. Sci Adv. 2020;6(18):eaaz6031. doi:10.1126/sciadv.aaz6031.

4. Service RF. Desalination freshens up. Science. 2006;313(5790):1088–90. doi:10.1126/science.313.5790.1088.

5. Qiu JX, Xu XY, Li Z, Hu YX, Liu GQ, Lv XM, et al. A solar-electric dual-driven microporous hydrogel evaporator for all-weather highly efficient water purification. Nano Energy. 2024;130:110057. doi:10.1016/j.nanoen.2024.110057.

6. Xu XY, Zhao Q, Liu Q, Qiu JX, Li J, Zheng WQ, et al. Full-spectrum-responsive Ti_4O_7-PVA nanocomposite hydrogel with ultrahigh evaporation rate for efficient solar steam generation. Desalination. 2024;577:117400. doi:10.1016/j.desal.2024.117400.

7. Zhao F, Guo YH, Zhou XG, Shi W, Yu GH. Materials for solar-powered water evaporation. Nat Rev Mater. 2020;5(5):388–401. doi:10.1038/s41578-020-0182-4.

8. Li Z, Qiu JX, Xu XY, Wan RT, Yao MT, Wang HB, et al. Solar driven kaolin-based hydrogels for efficient interfacial evaporation and heavy metal ion adsorption from wastewater. Sep Purif Technol. 2025;354:129243. doi:10.1016/j.seppur.2024.129243.

9. Zhou JH, Gu YF, Liu PF, Wang PF, Miao L, Liu J, et al. Development and evolution of the system structure for highly efficient solar steam generation from zero to three dimensions. Adv Funct Mater. 2019;29(50):1903255. doi:10.1002/adfm.201903255.

10. Zhao Q, Wu ZX, Xu XY, Yang RP, Ma HD, Xu QL, et al. Design of poly(3,4-ethylenedioxythiophene): polystyrene sulfonate-polyacrylamide dual network hydrogel for long-term stable, highly efficient solar steam generation. Sep Purif Technol. 2022;300:121889. doi:10.1016/j.seppur.2022.121889.

11. Zhao Q, Liu JY, Wu ZX, Xu XY, Ma HD, Hou JD, et al. Robust PEDOT: PSS-based hydrogel for highly efficient interfacial solar water purification. Chem Eng J. 2022;442:136284. doi:10.1016/j.cej.2022.136284.

12. Zhang QX, Zhang ZP, Zhao DY, Wang L, Li H, Zhang F, et al. Synergistic photocatalytic-photothermal contribution enhanced by recovered Ag^+ ions on MXene membrane for organic pollutant removal. Appl Catal B-Environ. 2023;320:122009. doi:10.1016/j.apcatb.2022.122009.

13. Su LF, Liu X, Xia W, Wu B, Li C, Xu B, et al. Simultaneous photothermal and photocatalytic MOF-derived C/TiO_2 composites for high-efficiency solar driven purification of sewage. J Coll Interf Sci. 2023;650:613–21. doi:10.1016/j.jcis.2023.07.014.

14. Wang ZY, Xu L, Liu CH, Han SJ, Fu ML, Yuan BL. MXene/CdS photothermal-photocatalytic hydrogels for efficient solar water evaporation and synergistic degradation of VOC. J Mater Chem A. 2024;12(18):10991–1003.

15. Fan DQ, Tang YC, Liao YM, Mi Y, Lu Y, Yang XF. Two birds with one stone: functionalized wood composites for efficient photocatalytic hydrogen production and solar water evaporation. Chin Chem Lett. 2024;35(9):109441. doi:10.1016/j.cclet.2023.109441.

16. Wang HW, Wang ZY, Wang T, Tang WQ, Gao SM, Niu H, et al. Shooting three birds with one stone: device construction and thermal management for simultaneous photothermal conversion water evaporation, thermoelectric generation and photocatalytic degradation. Adv Funct Mater. 2024;34(23):2315211. doi:10.1002/adfm.202315211.

17. Yu JW, Wan RT, Tian FJ, Cao J, Wang W, Liu Q, et al. 3D printing of robust high-performance conducting polymer hydrogel-based electrical bioadhesive interface for soft bioelectronics. Small. 2024;20(19):2308778. doi:10.1002/smll.202308778.

18. Yu JW, Tian FJ, Wang W, Wan RT, Cao J, Chen C, et al. Design of highly conductive, intrinsically stretchable, and 3D printable PEDOT: PSS hydrogels via PSS-chain engineering for bioelectronics. Chem Mater. 2023;35(15):5936–44. doi:10.1021/acs.chemmater.3c00844.

19. Wan RT, Yu JW, Quan ZY, Ma HD, Li JH, Tian FJ, et al. A reusable, healable, and biocompatible PEDOT: PSS hydrogel-based electrical bioadhesive interface for high-resolution electromyography monitoring and time-frequency analysis. Chem Eng J. 2024;490:151454. doi:10.1016/j.cej.2024.151454.

20. Hu Y. Biomedical DNA hydrogels. Soft Sci. 2022;2:3. doi:10.20517/ss.2021.20.

21. Liu C, Wang SJ, Feng SP, Fang NX. Portable green energy out of the blue: hydrogel-based energy conversion devices. Soft Sci. 2023;3:10.

22. Zhang ZL, Chen GD, Xue Y, Duan QF, Liang XY, Lin T, et al. Fatigue-resistant conducting polymer hydrogels as strain sensor for underwater robotics. Adv Funct Mater. 2023;33(42):2305705. doi:10.1002/adfm.202305705.

23. Luo XY, Wan RT, Zhang ZX, Song MT, Yan LX, Xu JK, et al. 3D-printed hydrogel-based flexible electrochromic device for wearable displays. Adv Sci. 2024;11:2404679. doi:10.1002/advs.202404679.

24. Ke XL, Mu XJ, Chen SY, Zhang ZX, Zhou JH, Chen YL, et al. Reduced graphene oxide reinforced PDA-Gly-PVA composite hydrogel as strain sensors for monitoring human motion. Soft Sci. 2023;3:21. doi:10.20517/ss.2023.14.

25. Li JH, Cao J, Lu BY, Gu GY. 3D-printed PEDOT: pSS for soft robotics. Nat Rev Mater. 2023;8(9):604–22. doi:10.1038/s41578-023-00587-5.

26. Zhao Q, Wen HK, Wu JY, Wen XL, Xu ZY, Duan JF. Galactomannan/graphene oxide/Fe_3O_4 hydrogel evaporator for solar water evaporation for synergistic photothermal power generation. Desalination. 2024;570:117064. doi:10.1016/j.desal.2023.117064.

27. Zheng DQ, Shi L, Zhang M, Huang WX, Li ZH, Long SF, et al. A self-floating and windproof Janus biomass composite hydrogel with magnetic controllability and salt rejection for polluted seawater desalination. Chem Eng J. 2024;497:154943. doi:10.1016/j.cej.2024.154943.

28. Lyu T, Wang ZY, Liu RN, Chen K, Liu H, Tian Y. Macroporous hydrogel for high-performance atmospheric water harvesting. ACS Appl Mater. 2022;14(28):32433–43. doi:10.1021/acsami.2c04228.

29. Li W, Liao GC, Duan W, Gao FF, Wang YS, Cui RX, et al. Synergistically electronic interacted PVDF/CdS/TiO_2 organic-inorganic photocatalytic membrane for multi-field driven panel wastewater purification. Appl Catal B-Environ. 2024;354:124108. doi:10.1016/j.apcatb.2024.124108.

30. Ghosh R, Baut A, Belleri G, Kappl M, Butt HJ, Schutzius TM. Photocatalytically reactive surfaces for simultaneous water harvesting and treatment. Nat Sustain. 2023;6(12):1663–72. doi:10.1038/s41893-023-01159-9.

31. Lou XX, Gao X, Liu Y, Chu MY, Zhang CY, Qiu YH, et al. Highly efficient photothermal catalytic upcycling of polyethylene terephthalate via boosted localized heating. Chin J Catal. 2023;49:113–22. doi:10.1016/S1872-2067(23)64435-3.

32. Ma JH, Xu L, Yin ZY, Li ZF, Dong XY, Song ZG, et al. One stone four birds design atom co-sharing BiOBr/Bi_2S_3 S-scheme heterojunction photothermal synergistic enhanced full-spectrum photocatalytic activity. Appl Catal B-Environ. 2024;344:123601. doi:10.1016/j.apcatb.2023.123601.

33. Zhang LJ, Jin ZL, Tsubaki N. Activating and optimizing the MoS_2@MoO_3 S-scheme heterojunction catalyst through interface engineering to form a sulfur-rich surface for photocatalyst hydrogen evolution. Chem Eng J. 2022;438:135238. doi:10.1016/j.cej.2022.135238.

34. Altan O, Altintas E, Alemdar S, Metin Ö. The rational design of a graphitic carbon nitride-based dual S-scheme heterojunction with energy storage ability as a day/night photocatalyst for formic acid dehydrogenation. Chem Eng J. 2022;441:136047. doi:10.1016/j.cej.2022.136047.

35. Xiong RZ, Ke XX, Jia WF, Xiao YH, Cheng BC, Lei SJ. Photothermal-coupled solar photocatalytic CO_2 reduction with high efficiency and selectivity on a MoO_3-x@$ZnIn_2S_4$core-shell S-scheme heterojunction. J Mater Chem A. 2023;11(5):2178–90. doi:10.1039/D2TA09255G.

36. Yu F, Luo CJ, Niu XH, Chao M, Zhang PF, Yan LK. An advanced 2D/3D g-C_3N_4/TiO_2@MnO_2 multifunctional membrane for sunlight-driven sustainable water purification. Nano Res. 2023;17(4): 2368–80. doi:10.1007/s12274-023-6071-6.

37. Yang CC, Zhang X, Zhou Y, Hao SX. Well-designed MOF-derived hollow octahedral structure TiO_2 coupled with ultra-thin porous g-C_3N_4 to enhance the degradation of real liquor brewing wastewater. Appl Surf Sci. 2023;616:156471. doi:10.1016/j.apsusc.2023.156471.

38. He PP, Lan HY, Bai HY, Zhu YY, Fan ZF, Liu J, et al. Rational construction of all-in-one metal-organic framework for integrated solar steam generation and advanced oxidation process. Appl Catal B-Environ. 2023;337:123001. doi:10.1016/j.apcatb.2023.123001.

39. Li PX, Yan XY, Gao SY, Cao R. Boosting photocatalytic hydrogen production coupled with benzyl alcohol oxidation over CdS/metal-organic framework composites. Chem Eng J. 2021;421:129870. doi:10.1016/j.cej.2021.129870.

40. Zhang BP, Wong PW, An AK. Photothermally enabled MXene hydrogel membrane with integrated solar-driven evaporation and photodegradation for efficient water purification. Chem Eng J. 2022;430:133054. doi:10.1016/j.cej.2021.133054.

41. Tao P, Ni G, Song CY, Shang W, Wu JB, Zhu J, et al. Solar-driven interfacial evaporation. Nat Energy. 2018;3(12):1031–41. doi:10.1016/j.nanoen.2022.108115.

42. Li R, Li Y, Jia XH, Yang J, Miao X, Shao D, et al. 2D/2D ultrathin polypyrrole heterojunct aerogel with synergistic photocatalytic-photothermal evaporation performance for efficient water purification. Desalination. 2024;574:117295. doi:10.1016/j.desal.2024.117295.

43. Jiang MM, Zheng RQ, Wang MJ, Li XQ. A MoS_2-based evaporator with porous structure and inter-layer channels for solar desalination and photocatalytic degradation. Sol Energy. 2024;279:112853. doi:10.1016/j.solener.2024.112853.

44. Shu L, Zhang XF, Yang ST, Qiu JH, Yao JF. Integration of CuS@MIL-100 into cellulose hydrogel for synergistic seawater desalination and photocatalytic decontamination. Sep Purif Technol. 2024;334:125971. doi:10.1016/j.seppur.2023.125971.

45. Yong ZJ, Yap LW, Fu RF, Shi QQ, Guo ZR, Cheng WL. Seagrass-inspired design of soft photocatalytic sheets based on hydrogel-integrated free-standing 2D nanoassemblies of multifunctional nanohexagons. Mater Horiz. 2021;8(9):2533–40. doi:10.1039/D1MH00753J.

46. Zhao YW, Zhang YJ, Liu AR, Wei ZZ, Liu SQ. Construction of three-dimensional hemin-functionalized graphene hydrogel with high mechanical stability and adsorption capacity for enhancing photodegradation of methylene blue. ACS Appl Mater. 2017;9(4):4006–14. doi:10.1021/acsami.6b10959.

47. Zhang W, Zhang YM, Liu Y. Cyclodextrin-cross-linked hydrogels for adsorption and photodegradation of cationic dyes in aqueous solution. Chem Asian J. 2021;16(16):2321–17. doi:10.1002/asia.202100535.

48. Huang DL, Li ZH, Zeng GM, Zhou CY, Xue WJ, Gong XM, et al. Megamerger in photocatalytic field: 2D g-C_3N_4 nanosheets serve as support of 0D nanomaterials for improving photocatalytic performance. Appl Catal B-Environ. 2019;240:153–73. doi:10.1016/j.apcatb.2018.08.071.

49. Wang Q, Wang T, Laila N, Huang K, Wang XW, Lei RB, et al. Carbon dots/TiO_2 enhanced visible light-assisted photocatalytic of leachate: simultaneous effects and Mechanism insights. Water Res. 2023;245:120659. doi:10.1016/j.watres.2023.120659.

50. Zhang LN, Liu TL, Liu TF, Hussain S, Li QY, Yang JJ. Improving photocatalytic performance of defective titania for carbon dioxide photoreduction by Cu cocatalyst with SCN-ion modification. Chem Eng J. 2023;463:142358. doi:10.1016/j.cej.2023.142358.